

Tropospheric Emission Spectrometer Nadir Spectral Radiance Comparisons

Mark W. Shephard¹, Helen M. Worden², Karen E. Cady-Pereira¹, Michael Lampel³, Mingzhao Luo², Kevin W. Bowman², Edwin Sarkissian², Reinhard Beer², David M. Rider², David C. Tobin⁴, Henry E. Revercomb⁴, Brendan M. Fisher², Denis Tremblay³, Shepard A. Clough¹, Gregory B. Osterman², Michael Gunson²

¹Atmospheric and Environmental Research (AER), Inc., Lexington, MA, USA

²Jet Propulsion Laboratory, Pasadena, CA, USA

³Raytheon Technical Services Co., Pasadena, CA, USA

⁴University of Wisconsin-Madison, USA

¹ Corresponding Author's Information:

Atmospheric and Environmental Research, Inc.

131 Hartwell Avenue, Lexington, MA 02421-3126, U.S.A.

Phone: 781-761-2288; Fax: 781-761-2299; e-mail: mshephar@aer.com

Abstract

The fundamental measurement of the Tropospheric Emission Spectrometer (TES) on board the Aura spacecraft is upwelling infrared spectral radiances. Accurate TES retrievals of surface and atmospheric parameters such as trace gas amounts critically depend on well-calibrated radiance spectra. On-orbit TES nadir observations were evaluated using carefully selected, nearly coincident spectral radiance measurements from AIRS-Aqua and special S-HIS underflights. Modifications to the L1B calibration algorithms for TES V002 data resulted in significant improvements for the TES-AIRS comparisons. The comparison of TES with S-HIS (adjusted for geometric differences) show mean and standard deviation differences of less than 0.3 K at warmer brightness temperatures of 290-295 K. The TES/S-HIS differences are less than 0.4 K at brightness temperatures of 265-270 K. There are larger TES/SHIS comparison differences for higher frequency TES 1A1 filter, which has less upwelling radiance signal. The TES/AIRS comparisons show mean differences of less than 0.3 K at 290-295 K and less than 0.5 K at 265-270 K with standard deviation less than 0.6 K for the majority of the spectral regions and brightness temperature range. A procedure to warm up the optical bench for better alignment in December 2005 gave a 4-fold increase in the SNR (signal-to-noise ratio) at higher frequency ranges. Recent results from a long-term comparison of TES SST (Sea Surface Temperature) observations with the ROI (Reynolds Optimally Interpolated) SST product demonstrate TES radiometric stability.

AGU Index Terms: 3360 Remote Sensing, 0360 Radiation: transmission and scattering, 0394

Instruments and techniques

1. Introduction

The Tropospheric Emission Spectrometer (TES) is a Fourier Transform Spectrometer (FTS) flying on the NASA Aura platform [Beer *et al.*, 2001; Beer, 2006, Schoeberl *et al.*, 2006]. The fundamental measurements used in the TES retrievals are the upwelling infrared spectral radiances. Thus, accurate radiances are critical for both trace gas profile retrievals for air quality as well as radiative forcing for climate [Gauss *et al.*, 2003]. For example, any radiometric systematic errors (e.g. calibration) not addressed in the L1B radiances will propagate as errors in the retrieved parameters [Bowman *et al.*, 2006, Worden *et al.*, 2004]. The quality of the TES spectra has improved significantly since launch in July 2004; it is the purpose of this paper to provide a brief overview of the improvements and benchmark the current radiometric accuracy, principally through comparisons with instruments whose accuracy is well documented.

TES has a number of observational modes (e.g. Global Survey, Step-and-Stare, Transect). In Global Survey mode TES makes measurements along the satellite track for 16 orbits with a spacing of ~ 182 km; in Step-and-Stare mode nadir measurements are made every 40 km along the track for approximately 50 degrees of latitude; in Transect mode observations consist of series of 40 consecutive scans spaced 12 km apart. TES also has the capability to perform both nadir and limb viewing, but for the validations presented here we have focused on the nadir-viewing mode. TES nadir spectra have 0.06 cm^{-1} unapodized spectral resolution and have footprints of $8 \times 5\text{ km}^2$ resulting from the averages of 16-element detector arrays where each detector has a $0.5 \times 5\text{ km}^2$ nadir footprint. Figure 8 is an example of the TES nadir spectrum from November 7, 2004.

TES L1B processing produces radiometrically and spectrally calibrated radiance spectra from L1A interferograms. Interferograms for calibration targets, i.e., the reference blackbody at 340K and a view of cold space, are taken routinely so that nadir and limb earth views are bracketed in time with calibration measurements. For Global Survey observations, the time span between calibrations is 82 seconds and calibration scans are included in an optimal fit for time variability that also reduces their noise contribution through averaging. For special observations, the time spans are longer: 7.5 minutes for the Transect mode and 17 minutes for the Step-and-Stare mode. Special observations use a linear-in-time interpolation of scan averages taken before and after the target observations. Based on studies of calibration stability, a linear interpolation over these bracketing time scales is sufficient to capture changes in the instrument-offset radiance.

To calibrate an individual target scan with averaged, time interpolated cold space and blackbody spectra, the TES calibration algorithm follows the methods first proposed by *Revercomb et al.* [1988a] using complex calibration and target spectra to explicitly remove instrument phase errors. The TES L1B algorithm is described in detail in the Algorithm Theoretical Basis Document (ATBD) [*Worden and Bowman*, 1999] and results from the instrument-commissioning phase are given in *Worden et al.* [2006].

In order to ascertain the quality of the TES radiances, comparisons were made between TES spectra and measurements from two other spectrometers, the Atmospheric Infrared Sounder (AIRS) on NASA's Aqua satellite [*Aumann et al.*, 2003] and the Scanning High-Resolution Interferometer Sounder (S-HIS) flown on an aircraft. AIRS measures 2378 infrared radiances between 650 and 2665 cm^{-1} with a resolving power ($\lambda/\Delta\lambda$) of 1200 (e.g. 0.5 cm^{-1} at 600 cm^{-1} ; 2.0 cm^{-1} at 2400 cm^{-1}). Brightness temperature comparisons of AIRS with S-HIS show the AIRS

radiometric accuracies to be ~ 0.2 K for most channels [Tobin *et al.*, 2006]. The S-HIS design and calibration techniques have developed from experience with the HIS and from the ground based Atmospheric Emitted Radiance Interferometer (AERI) instruments developed for the DOE Atmospheric Radiation Measurement (ARM) program [Revercomb *et al.* 1988a, 1988b, 1996]. For a description of the calibration approach and algorithms used for AERI, which are similar to S-HIS, the reader is referred to Knuteson *et al.* [2004a, 2004b]. The S-HIS has programmable cross-track scanning with ~ 2 km footprints when flying on an aircraft near the tropopause. The focus of the design of the S-HIS has been on obtaining accurate calibration, and perturbation analysis of the radiometric calibration shows that the S-HIS has absolute radiometric uncertainties of less than 0.15 K for scene brightness temperatures greater than 250 K.

In Section 2.1 comparisons between TES and AIRS are used to highlight the increased accuracy in the TES spectra due to changes in the TES L1B algorithm (V001 to V002). In Section 2.2 the improvement in the TES 1A1 band obtained through an optical bench warm up is discussed. In Section 3, S-HIS and AIRS radiance comparisons are used to validate the TES spectra. Section 4 presents an overview of TES sea surface temperature (SST) comparisons, which are used to show the long-term stability of the TES radiances.

2. TES Radiance Updates

2.1 TES L1B Algorithm Improvements

Significant improvements to the L1B algorithms were made between data versions V001 and V002. The most significant updates are to the modeling the time dependence, and the improved sampling phase alignment. These changes included a more robust approach to the

correction for the ambiguous linear sampling phase that can be different between scans and must be aligned before averaging and complex calibration can be performed. The complex calibration was computed using Equation (1):

$$L_{T_{\text{arg et}}} = \frac{C_{T_{\text{arg et}}} - C_{CS}}{C_{BB} - C_{CS}} \epsilon_{BB} B(T_{BB}), \quad (1)$$

where, $L_{T_{\text{arg et}}}$ is the calibrated TES target radiance, $C_{T_{\text{arg et}}}$ complex target spectrum, C_{CS} complex cold space view spectrum, C_{BB} complex blackbody spectrum, ϵ_{BB} blackbody emissivity, and the Planck function for the blackbody $B(T_{BB})$ at temperature T . Note that the contribution of the cold space blackbody ($\sim 3\text{K}$) is negligible. The optimal fit for time variability in Global Surveys calibration data was also included for V002 data. The most significant source of time variability over a Global Survey was the build-up of ice on the detector arrays (which is removed by decontamination cycles).

Since the AIRS-Aqua is just 15 minutes ahead of TES-Aura on the ‘‘A-Train’’ orbit, TES comparisons with AIRS spectra were used as a metric for algorithm improvements. For the TES/AIRS comparison, 190 TES nadir targets from Global Survey 2147 (16-orbits) on September 20, 2004 that have a 0.5 K homogeneity in surface brightness temperatures across a detector array were identified. Of these 50, were confirmed as homogenous for AIRS also, as determined by the AIRS spatial uniformity tests discussed in *Aumann et al.*, [2006]. These homogenous nadir targets are the cases for TES L1B algorithm improvements used for TES V002. Figure 1 shows the improvement in the TES/AIRS ratio in the V002 (Panel B) calibration as compared with V001 (Panel A). For the TES/AIRS comparison, the high-resolution TES spectrum was convolved directly with the lower resolution AIRS SRF (spectral response function) provided for each AIRS channel. This direct application of the AIRS SRF to TES data,

essentially assuming the TES spectrum is monochromatic, is accurate to within 0.002 K [Sarkissian *et al.*, 2005].

Figure 2 - Figure 4 show the frequency and time dependence of TES-AIRS comparisons for TES 2B1, 1B2 and 2A1 filters. These figures show results for single pixel comparisons. For each filter, the top panel shows the average over 50 nadir targets of the TES-AIRS brightness temperature difference as a function of frequency on the AIRS frequency grid. The bottom panels show averages over frequency as a function of target index or time, spanning about 26 hours. These plots demonstrate how the different V002 improvements affect the TES frequency ranges. In the 2B1 filter, the most significant improvement is from modeling the time dependence, while in 1B2 and 2A1, the time dependence is nearly flat in both the baseline and prototype runs, as expected from the spectral dependence of ice absorption which has a broad peak centered around 830 cm^{-1} . For 1B2, and especially 2A1, we see large improvements due primarily to the improved sampling phase alignment. Table 1 contains V001 and V002 full filter averaged statistics for Global Survey 2147. Also included in the table are comparison results from Global Survey 2931 on May 21, 2005, which had 320 match-up target scenes. Note that the statistics in Table 1 are computed using TES 16-pixel scenes. These V002 L1B modifications have resulted in improved TES retrieval parameters as demonstrated, for example, in sea surface temperature retrievals, for V001 data vs. V002 data [Tremblay *et al.*, this issue], and in ozonesonde comparisons for V001 data [Worden *et al.*, 2007] vs. V002 data [Nassar *et al.*, this issue]. Comparison results in the TES 1A1 filter are not shown here as these L1B improvements had much less impact on this band due to the very small contribution of the instrument background radiance at those frequencies. In addition, the overlap region between TES and AIRS in this filter is very small ($2181\text{-}2251\text{ cm}^{-1}$) and covers a spectral region not used

for TES retrievals as it can contain a significant amount of unusable TES spectral “spikes” that are not easily identified at these low radiances. Analysis of the frequencies and amplitudes of the TES spectral spikes points directly to electromagnetic pickup of the analog-to-digital converter-sampling clock by the signal chains [Beer *et al.*, 2003]. The main improvement for radiances in the 1A1 filter was obtained from the on-orbit optical bench warm-up.

2.2 TES Instrument Improvements: Optical Bench Warm-Up

The optical bench warm-up was used to adjust and maintain the alignment of the instrument beam-splitter, thus increasing the integrated spectral magnitude (ISM). The ISM is calculated as the integration of the raw spectrum for a given filter when the instrument views the on-board 340 K blackbody calibration source. The ISM calculation is performed routinely providing a sensitive measure of the trend in the mean signal levels at the detector. Figure 5 contains a plot of normalized Integrated Spectral Magnitude (ISM) that has been updated from the one presented in Rinsland *et al.* [2006] to cover the time period from launch until March, 2007. From launch until the optical bench warm-up, which took place between November 29 and December 2, 2005, there was a steady drop in ISM. The periodic jumps in the ISM corresponded to small increases in the optical bench temperature during routine decontamination for ice buildup, which was needed more frequently at the beginning of a mission. These increases confirmed the results from pre-launch calibration that the beam-splitter alignment could be adjusted by changing the temperature of the optical bench. The optical bench warm-up of 6K resulted in an increase of a factor of 3.4 in the ISM. This improvement has a significant impact on retrievals using the 1A1 filter. For example, Rinsland *et al.* [2006] showed that the degrees of

freedom for signal (DOFS), which is a measure of the number of independent pieces of information obtained in the retrieval [Rodgers, 2000], for CO increased by a factor of 2 (0.72 to 1.45 averaged for 30S – 30N) after the optical bench warm-up. Unfortunately there are no good comparison observations available for an external evaluation of the radiometric accuracy after the improvements due to the optical bench warm-up. This is because AIRS does not have overlapping frequencies with the TES 1A1 filter in a region that is useful for comparisons and there are currently no available SHIS underpasses observations in cloud-free conditions after the optical bench warm-up. However, in order to provide additional metrics on the impact of the optical bench warm-up we compare noise equivalent spectral brightness temperature (NESBT) for TES filter 1A1 before and after the optical bench warm-up. NESBT is computed from the noise equivalent spectral radiance (NESR) by adding it to the Planck function for the average spectral brightness temperature, converting from radiance to brightness temperature and subtracting off the average spectral brightness temperature. Figure 6 shows the NESBT plots for: (i) Run 3194, a TES global survey on November 27-28, 2005 just before the optical bench warm-up; (ii) Run 3202, a TES global survey on December 7-8, 2005 just after the optical bench warm-up; and (iii) Run 2298, which is the TES step-and-stare run used in the TES/SHIS comparisons and provided for reference. Comparing TES observations just before (run 3194) and after (run 3202) provides an estimate of the noise improvements in the TES 1A1 filter obtained from the optical bench warm-up. Note that the NESBT values in Figure 6 are likely an overestimate of the noise due to unidentified spikes being included in the calculations.

3. Radiance Validations

TES nadir spectral radiances have been validated against both SHIS and AIRS. Here we show examples of the radiance comparisons used to validate the TES observed radiances.

3.1 TES/S-HIS Radiance Comparison

During the Aura Validation Experiment (AVE) there were several S-HIS underflights of TES. We studied two cloud-free scans on November 7, 2004 where S-HIS flew under the TES overpass at an altitude of 18 km over the Gulf of Mexico. The absence of clouds is determined by the zero cloud fraction retrieved by the Moderate Resolution Imaging Spectroradiometer (MODIS) and by the small variability in the 1103-1105 cm^{-1} window brightness temperatures demonstrated in the TES and S-HIS scans in Figure 7. The brightness temperatures plotted here have not been corrected for any geometric difference between the two sensors, therefore, given that TES is flying at a much higher altitude the TES brightness temperatures in the window region are expected to be cooler. An average TES spectrum for each scan was obtained by averaging the sixteen TES pixels; a corresponding SHIS spectrum was constructed by averaging the nine closest SHIS scans to the center of the TES scan. The SHIS footprints in Figure 7 show the SHIS scans used in the comparisons. Unfortunately, there were no coincident AIRS observations available at this time.

In order to compare the spectra from the different instruments Line-by-Line Radiative Transfer Model (LBLRTM) (*Clough et al.*, 2005) forward model calculations were utilized to account for the differences between altitude and viewing angles (see Equation (2)).

$$[\text{TES} \star \text{SHIS ILS} - ((\text{LBLRTM} \star \text{TES ILS}) \star \text{SHIS ILS})] - [\text{SHIS} - (\text{LBLRTM} \star \text{SHIS ILS})] \quad (2)$$

The \star in Equation (2) is the convolution operator. This follows the approach used to provide accurate and detailed assessment of the AIRS spectral radiance observations [Tobin *et al.*, 2006]. Implicit in this procedure is the assumption that the modeled atmosphere between the aircraft altitude and the satellite is representative of the true atmosphere. When the atmosphere specified above the nadir S-HIS observation (18 km) does not represent the true atmospheric state there will be additional residuals in the spectral regions where there is emission above the aircraft.

TES and S-HIS have spectral resolutions of 0.06 cm^{-1} and 0.48 cm^{-1} , respectively. In order to put the two sensors on the same resolution for comparison purposes, TES was convolved with S-HIS Instrument Line Shape (ILS). Figure 8 shows a TES, S-HIS, and TES spectra convolved with the S-HIS ILS (TES \star SHIS ILS) for TES Run 2298, Sequence 3, Scan 10 on November 7, 2004. Noticeable differences between TES and SHIS are evident in the spectral regions where there is significant emission above the aircraft (e.g. CO_2 and O_3 spectral regions). An example of the TES-S-HIS spectral comparisons, as defined by Equation (2), for the 2B1, 1B2, 2A1, and 1A1 TES filters for Scan 10 are shown in Figure 9. Note that more detailed TES spike remove was performed on the TES observations for these comparisons because the full-filter forward model calculations used to account for the geometric differences in Equation (2) were also used to further identify TES spikes; any 4-sigma (TES-LBLRTM) spectral points were removed from the statistics. Over most of the TES spectral regions there is good agreement with S-HIS. The largest residuals are in the regions with significant emission above the aircraft (e.g. $\text{CO}_2 \nu_2$ ($\sim 650\text{-}700 \text{ cm}^{-1}$ in the 2B1), O_3 ($1020\text{-}1060 \text{ cm}^{-1}$ in the 1B2), $\text{CH}_4 \nu_4$ (Q-branch at 1306 cm^{-1} in the 2A1), and the start of the $\text{CO}_2 \nu_3$ (the $2180\text{-}2251 \text{ cm}^{-1}$ in the 1A1)). As stated earlier, incorrect specification of the atmosphere above the aircraft will result in differences beyond the differences in the instrument radiances themselves. In addition, incorrect specification of the

atmosphere in a region in which one sensor is more sensitive to than the other will also generate differences that are not due to radiances themselves. For example, a sensor flying on an aircraft will in general be more sensitive to the atmosphere just below the aircraft than an instrument observing from space (e.g. temperature and ozone). Since there were no coincident and collocated sonde profiles available to specify the atmosphere state, the TES retrieved profile was used in the calculations. The TES *a priori* profile calculated from the GEOS global transport model maintained at NASA's Global Modeling and Assimilation Office (GMAO) [Bloom *et al.*, 2005] was tried (not shown), however it did not characterize the atmosphere as well as the TES retrieved profile.

Additional insight from these comparisons is obtained from scatter plots of the combined brightness temperature differences from both Scans 8 and 10 as a function of brightness temperature (Figure 10). There are small but systematic differences between the TES and S-HIS at warmer temperatures near the surface (285-300 K); filter 2B1 has a difference of -0.2 K, 1B2 of -0.28 K, 2A1 differences are very close to zero, and the 1A1 band has a systematic difference of 0.5K. The 2B1 differences become slightly positive at wavenumbers below 700 cm^{-1} , where emission is mainly from the tropopause region. The 1B2 differences show a distinctive increase with decreasing temperature and wavenumber, as the emission moves into the O_3 band. Detailed TES-SHIS comparison statistics for 5K temperature bins at 265-270 K and 290-295 K are in Table 2. It should be pointed out that the signal in the 1A1 region is low due to the cold temperatures and drop-off in radiance of the blackbody plank function at these wavenumbers and temperatures. Therefore, differences due to noise or spikes in the TES radiances will result in large brightness temperature differences in the 1A1 filter, especially at the high frequencies and cooler temperatures.

3.2 TES/AIRS Radiance Comparison

A different perspective on the TES-AIRS differences can be obtained from the same dataset presented in Section 2.1 by plotting the TES-AIRS residuals as a function of the TES brightness temperature and frequency (Figure 11). For this analysis only clear sky scenes over ocean were used; a scene was determined to be clear using brightness temperature inter-pixel variability (16-pixel standard deviation <0.25 K), absolute brightness temperature (greater than 273 K), and the lapse rate (greater than 3° C/km). Each of the bands reveals an interesting aspect of the TES-AIRS differences. The 2B1 differences are close to zero across most of the band (from the surface to the tropopause) and become negative at cooler temperatures in the part of the CO_2 ν_2 ($650\text{-}680\text{ cm}^{-1}$) band where the emission is mainly from the tropopause and above. The 1B2 differences are also zero near the surface, but become positive (0.3 K to 0.4 K) at the cooler temperatures associated with the ozone stratospheric emission ($1020\text{-}1040\text{ cm}^{-1}$). Finally, the residuals in the 2A1 band are approximately constant over the entire band with average difference values between 0.3 K and 0.5 K, even at the surface, where the residuals in 2B1 and 1B2 are zero. Some of the TES-AIRS comparison differences maybe attributed to the fact that the two observations may not be observing exactly the same atmosphere (e.g. water vapor, unscreened clouds, etc.) as they are not simultaneous measurements (15-minutes apart) and have different field-of-views. Detailed statistics for 5 K temperature bins at 265-270 K and 290-295 K can be found in Table 2. The TES-AIRS standard deviations are larger than the TES-SHIS reported in Table 2. This might be due to the fact that TES-AIRS comparison covers a wider range of atmospheric states than the TES-SHIS comparison, and/or that SHIS is a better-

calibrated instrument, especially when you consider that nine SHIS footprints are averaged together in one TES scene.

4. TES Radiance Validation from SST Measurements

In addition to direct AIRS and S-HIS radiance comparisons, TES radiances can be indirectly validated through comparisons of retrieved sea surface temperature (SST) (e.g. *Hagan and Minnett*, 2003; *Aumann et al.*, 2006). These SST comparisons by *Tremblay et al.* [this issue] for clear sky radiances (retrieved effective cloud optical depth ≤ 0.05) over two years, demonstrates the long-term stability of TES measurements. It is important to note that the DOFS for the SST retrievals are generally close to 1 for these clear sky cases and therefore the TES SSTs are not biased by the *a priori*. *Tremblay et al.*, [this issue] shows the time series of the SST bias with respect to Reynolds Optimally Interpolated (ROI) monthly average SST from November 2004 through November 2006 for nighttime and daytime. The ROI dataset has the advantage that it is insensitive to clouds. In addition, the ROI is a bulk SST measurement allowing for a skin-bulk SST comparison, which can be used to determine the sensitivity of the TES SST retrievals. The average nighttime bias over this period is -0.17 K and the daytime average bias is 0.04 K, which is the expected difference between skin (TES) and bulk (ROI) temperature measurements. This ability to measure a skin-bulk temperature difference that is consistent with the expected physical skin-bulk nighttime bias of ~ 0.2 K, clearly shows that TES has a sensitivity at the 0.1 K level. RMS differences of ~ 0.5 K are consistent with the other comparison results shown in this paper. These results demonstrate that TES calibration has been very stable over the two-year period. It is also important to note that *Tremblay et al.*, [this issue] provides further evidence that the *a priori* does not bias the SST retrievals under clear sky

conditions. They provide a case study in which the *a priori* surface temperatures over Lake Tahoe were 17 K higher than the retrieved values (due to the fact that land surface temperature were used instead of water surface temperatures), however, the retrieved surface temperatures still compare quite well with the in-situ measurements with a bias of -0.11 K and standard deviation of 0.30 K.

5. Discussion and Concluding Remarks

Radiance comparison case studies of TES with S-HIS and AIRS are utilized to estimate the in-orbit radiometric calibration of TES. The mean and standard deviation of TES differences with both AIRS and SHIS are presented. TES/S-HIS comparisons show a mean difference of less than 0.3 K with a standard deviation of 0.3 K for brightness temperatures at 290-295 K, except for the 1A1 filter where the reduced signal increases the brightness temperature differences. Note that TES comparisons with both AIRS and S-HIS at these warmer brightness temperatures (near the surface) show that the 2B1 and 1B2 filters agree with each other, but the 2A1 filter is 0.2-0.3 K warmer. If not taken into consideration this systematic error will impact retrievals that use multiple filters (e.g. TES cloud retrieval). The TES/S-HIS comparison results for cooler brightness temperatures show mean differences less than 0.2 K with standard deviation less than 0.4 K at 265-270 K. Since some of these comparisons at the cooler brightness temperatures are from spectral regions where there is significant contribution from the atmospheric emission, it is likely that the differences are greater than the differences in the instrument radiances themselves due to errors in the input profiles used to account for the atmosphere between the aircraft. The TES/AIRS comparison show a mean difference of less

than 0.3K with a standard deviation of 0.6 K at brightness temperatures 290-295 K. Comparisons at cooler brightness temperatures 265-270 K show TES/AIRS mean and standard deviation differences of 0.5 K and 0.6 K, respectively.

It must be noted that TES calibration errors increase significantly within about 10 cm^{-1} of the half-power point frequencies of the optical filters. A study by *Revercomb et al.* (unpublished data, 2006) suggests the errors are likely due to a phase modulation resulting from interferometer velocity variations. These errors are mitigated in the L2 retrieval by the selection of frequency ranges that do not include the filter edges. Table 3 lists the useable spectral ranges that were determined based on the radiance comparisons.

Even though great efforts have been made to obtain coincident and co-located radiance observations under conditions in which the true state of the atmosphere is known, this is a challenging task. In addition, TES radiance validation is on going since instrument properties can change over the mission lifetime. Future radiance comparisons (e.g. with S-HIS) under cloud-free conditions, over water (where the infrared emissivity is well known), and where the atmosphere has been well characterized (e.g. radiosondes, ozonesondes, etc.) would be extremely useful for this validation effort. In addition, TES/AIRS radiance comparison results can be further refined in the future by including more comparison. This article has focused on nadir observations that have a greater potential for coincident measurements. Validation of TES limb radiances will rely heavily on model comparisons and will be addressed in a future publication.

370

371 **Acknowledgments.**

372

373 We would like to thank Eli Mlawer and Ted Kennelly at AER for their helpful
374 discussions. We would also like to thank George Aumann (JPL) for supplying us with AIRS
375 match-up data. We would also like to thank the reviewers and the associate editor for their very
376 constructive comments. This work was supported by the Jet Propulsion Laboratory, California
377 Institute of Technology, under a contract with the National Aeronautics and Space
378 Administration. Part of the TES Aura data used in this research was obtained from the NASA
379 Langley Research Center Atmospheric Sciences Data Center. The AQUA MODIS cloud data
380 was obtained from NASA's L1 and Atmospheric Archive and Distribution System (LAADS
381 WEB) website (<http://ladsweb.nascom.nasa.gov/>).

References

- Aumann, H. H., S. Broberg, D. Elliott, S. Gaiser, and D. Gregorich (2006), Three years of AIRS radiometric calibration validation using sea surface temperatures, *J. Geophys. Res.*, *111*, doi:10.1029/2005JD006822.
- Aumann, H. H., M. T. Chahine, C. Gautier, M. D. Goldberg, E. Kalnay, L. M. McMillin, H. Revercomb, P. W. Rosenkranz, W. L. Smith, D. H. Staelin, L. L. Strow, and J. Susskind (2003), AIRS/AMSU/HSB on the Aqua mission: design, science objectives, data products, and processing systems, *IEEE Trans. Geosci. Remote Sensing*, *41*, 253-264.
- Beer, R. (2006), TES on the Aura Mission: Scientific Objectives, Measurements and Analysis Overview, *IEEE Trans. Geosci. Remote Sensing*, *44*(5), 1102.
- Beer, R., K. W. Bowman, B. M. Fisher, M. R. Gunson, R. G. Holm, M. Luo, D. M. Rider, E. Sarkissian, S. S. Kulawik, D. A. Tremblay, and H. M. Worden (2003), Tropospheric Emission Spectrometer Instrument Calibration Report, *Volume 1 and 2*, JPL, Pasadena, CA, USA, D-26533 (<http://tes.jpl.nasa.gov>).
- Beer, R., T. A. Glavich, and D. M. Rider (2001), Tropospheric emission spectrometer for the Earth Observing System's Aura satellite, *Appl. Optics*, *40*, 2356-67.
- Bloom, S., A. da Silva, D. Dee, M. Bosilovich, J.-D. Chern, S. Pawson, S. Schubert, M. Sienkiewicz, I. Stajner, W.-W. Tan, and M.-L. Wu (2005), Documentation and Validation of the Goddard Earth Observing System (GEOS) Data Assimilation System – Version 4. Technical Report on Global Modeling and Data Assimilation 104606, 26. Available from

<http://gmao.gsfc.nasa.gov/pubs/docs/Bloom168>.

Bowman K. W., C. D. Rodgers, S. S. Kulawik, J. Worden, E. Sarkissian, G. Osterman, T. Steck, M. Lou, A. Eldering, M. Shephard, H. Worden, M. Lampel, S. A. Clough, P. D. Brown, C. P. Rinsland, M. Gunson, and R. Beer (2006), Tropospheric emission spectrometer: Retrieval method and error analysis, *IEEE Trans. Geosci. Remote Sens.*, 44(5), 1297-1307.

Clough, S. A., M. W. Shephard, E. J. Mlawer, J. S. Delamere, M. J. Iacono, K. Cady-Pereira, S. Boukabara, and P. D. Brown (2005), Atmospheric radiative transfer modeling: a summary of the AER codes, Short Communication, *J. Quant. Spectrosc. Radiat. Transfer*, 91, 233-244.

Gauss M., G. Myhre, G. Pitari, M. J. Prather, I. S. A. Isaksen, T. K. Berntsen, G. P. Brasseur, F. J. Dentener, R. G. Derwent, D. A. Hauglustaine, L. W. Horowitz, D. J. Jacob, M. Johnson, K. S. Law, L. J. Mickley, J.-F. Muller, P.-H. Plantevin, J. A. Pyle, H. L. Rogers, D. S. Stevenson, J. K. Sundet, M. van Weele, and O. Wild (2003), Radiative forcing in the 21st century due to ozone changes in the troposphere and the lower stratosphere. *J. Geophys. Res.*, 108(D9), 4292.

Hagan, D., and P. Minnett (2003), AIRS Radiance Validation Over Ocean From Sea Surface Temperature Measurements, *IEEE Trans. Geosci. Remote Sensing*, 41, 432-441, 2003.

Knuteson, R. O., H. E. Revercomb, F. A. Best, N. C. Ciganovich, R. G. Dedeker, T. P. Dirkx, S. C. Ellington, W. F. Feltz, R. K. Garcia, H. B. Howell, W. L. Smith, J. F. Short, and D. C. Tobin (2004a), Atmospheric Emitted Radiance Interferometer. Part I: Instrument Design, *J. Atmos. Ocean. Tech.*, 21, 1763-1776.

- 425 Knuteson, R. O., H. E. Revercomb, F. A. Best, N. C. Ciganovich, R. G. Dedecker, T. P. Dirkx, S.
 426 C. Ellington, W. F. Feltz, R. K. Garcia, H. B. Howell, W. L. Smith, J. F. Short, and D. C.
 427 Tobin (2004b), Atmospheric Emitted Radiance Interferometer. Part II: Instrument
 428 Performance, *J. Atmos. Ocean. Tech.*, *21*, 1777-1789.
- 429 Nassar, R., J. Logan, H. Worden, I. Megretskaya, et al. (2007), Validation of Tropospheric
 430 Emission Spectrometer (TES) Nadir Ozone Profiles Using Ozone Sonde Measurements, *J.*
 431 *Geophys. Res.*, (this issue).
- 432 Revercomb, H., D. L. Buijs, H. B. Howell, W. Smith, and L. Sromovsky (1988a), Radiometric
 433 calibration of IR Fourier transform spectrometers: solution to a problem with the high-
 434 resolution interferometer sounder, *Appl. Opt.*, *27*, 3210.
- 435 Revercomb, H. E., D. D. LaPorte, W. L. Smith, H. Buijs, D. G. Murcray, F. J. Murcray, and L.A.
 436 Sromovsky (1988b), High-Altitude Aircraft Measurements of Upwelling IR Radiance:
 437 Prelude to FTIR from Geosynchronous Satellite, *Mikrochimica Acta [Wien]*, *II*, 439-444.
- 438 Revercomb, H. E., W. L. Smith, F. A. Best, J. Giroux, D. D. LaPorte, R. O. Knuteson, M. W.
 439 Werner, J. R. Anderson, N. N. Ciganovich, R. W. Cline, S. D. Ellington, R. G. Dedecker,
 440 T. P. Dirkx, R. K. Garcia, and H. B. Howell (1996), Airborne and ground-based Fourier
 441 transform spectrometers for meteorology: HIS, AERI and the new AERI-UAV.
 442 *Proceedings SPIE Optical Instruments for Weather Forecasting*, ed. G.W. Kamerman,
 443 2832, 106-117.
- 444 Rinsland, C. P., M. Luo, J. A. Logan, R. Beer, H. Worden, S. Kulawik, D. Rider, G. Osterman,
 445 M. Gunson, A. Goldman, M. Shephard, S. A. Clough, C. Rodgers, M. Lampel, and L. Chiou

(2006), Nadir Measurements of Carbon Monoxide (CO) Distributions by the Tropospheric Emission Spectrometer Instrument onboard the Aura Spacecraft: Overview of Analysis Approach and Examples of Initial Results, *Geophys. Res. Lett.*, *33*, L22806, doi:10.1029/2006GL027000.

Rodgers, C. D. (2000), Inverse Methods for Atmospheric Sounding: Theory and Practice. World Scientific.

Sarkissian E., H. M. Worden, K. W. Bowman, B. Fisher, D. Rider, H. H. Aumann, M. Apoliniski, R. C. Debaca, S. Gluck, M. Madatyan, J. McDuffie, D. Tremblay, M. W. Shephard, K. E. Cady-Pereria, D. Tobin, and H. Revercomb (2005), "TES Radiometric Assessment", AGU Meeting, San Francisco, December 5-9.

Schoeberl, M. R., et al. (2006), Overview of the EOS Aura Mission, *IEEE Trans. Geosci. Remote Sens.*, *44*(5), 1066-1074.

Tobin, D.C., H. E. Revercomb, R. O. Knuteson, F. A. Best, W. L. Smith, N. N. Ciganovich, R. G. Dedecker, S. Dutcher, S. D. Ellington, R. K. Garcia, H. B. Howell, D. D. LaPorte, S. A. Mango, T. S. Pagano, J. K. Taylor, P. van Delst, K. H. Vinson, and M. W. Werner (2006), Radiometric and spectral validation of Atmospheric Infrared Sounder observations with the aircraft-based Scanning High-Resolution Interferometer Sounder, *J. Geophys. Res.*, *111*, D09S02, doi:10.1029/2005JD006094.

Tremblay et al. (2007), Validation of Tropospheric Emission Spectrometer (TES) Water Surface Temperature, submitted to *J. Geophys. Res.*, (this issue).

- 467 Worden, H. M., and K. W. Bowman (1999), Tropospheric Emission Spectrometer (TES) Level
468 1B Algorithm Theoretical Basis Document (ATBD), V. 1.1, *JPL D-16479*, Oct. 1999,
469 available at: <http://eospso.gsfc.nasa.gov/atbd/testables.html>.
- 470 Worden, H., R. Beer, K. Bowman, B. Fisher, M. Luo, D. Rider, E. Sarkissian, D. Tremblay, and
471 J. Zong (2006), TES level1 algorithms: interferogram processing, geolocation, radiometric
472 and spectral calibration, *IEEE Trans. Geosci. Remote Sensing*, *44*(5), 1288-1296.
- 473 Worden, H. M., J. A. Logan, J. R. Worden, R. Beer, K. Bowman, S. A. Clough, A. Eldering, B.
474 M. Fisher, M. R. Gunson, R. L. Herman, S. S. Kulawik, M. C. Lampel, M. Luo, I. A.
475 Megretskaia, G. B. Osterman, and M. W. Shephard (2007), Comparisons of Tropospheric
476 Emission Spectrometer (TES) ozone profiles to ozonesondes: Methods and initial results, *J.*
477 *Geophys. Res.*, *112*, D03309, doi:10.1029/2006JD007258.
- 478 Worden, J., S. S. Kulawik, M. W. Shephard, S. A. Clough, H. M. Worden, K. Bowman, and A.
479 Goldman (2004), Predicted errors of Tropospheric Emission Spectrometer nadir retrievals
480 from spectral window selection, *J. Geophys. Res.*, *109*, D09308.
- 481

Table 1. TES V001 and V002 full-filter radiance comparisons

		TES-AIRS			
		Run 2147 9/20/2004 (50 target scenes)		Run 2931 5/21/2005 (320 target scenes)	
TES Filter	Wavenumber (cm ⁻¹)	Mean Δ BT (K)	STD Δ BT (K)	Mean Δ BT (K)	STD Δ BT (K)
2B1	650 - 920	-0.18 (-0.29)	0.46 (0.86)	-0.13 (-0.31)	0.42 (0.54)
1B2	920 - 1160	0.01 (-0.05)	0.48 (0.52)	-0.12 (-0.19)	0.38 (0.38)
2A1	1090 - 1340	0.34 (1.05)	0.36 (0.37)	0.35 (1.37)	0.32 (0.70)
<p>The evaluation statistics are averaged over the full filter.</p> <p>The values in ()'s are from TES V001 release.</p>					

Table 2. TES V002 Clear-sky radiance comparisons with AIRS and S-HIS

			TES - AIRS		TES - S-HIS	
			Run 2147 9/20/2004 (43 clear-sky scenes)		2298 0003 08 and 2298 0003 10 11/07/2004	
TES Filter	Wavenumber (cm ⁻¹)	Bright. Temp. (K)	Mean Δ BT (K)	STD Δ BT (K)	Mean Δ BT (K)	STD Δ BT (K)
2B1	650 – 920	290-295	-0.07	0.61	-0.19	0.27
		265-270	0.08	0.56	0.03	0.35
1B2	920 – 1160	290-295	-0.02	0.50	-0.28	0.15
		265-270	0.44	0.45	-0.04	0.21
2A1	1090 – 1340	290-295	0.26	0.59	0.02	0.18
		265-270	0.49	0.41	-0.11	0.36
1A1	1891 - 2251	290-295			0.56	0.94
		265-270			1.03	1.73

The statistics are for 1-sigma.

488

489 **Table 3. Spectral ranges for TES filters commonly used in the nadir**

Filter ID	L1B min.	L1B max.	Suggested min. for L2	Suggested max. for L2
2B1	652	919	660	910
1B2	923	1160	950	1130
2A1	1090	1339	1120	1320

490

List of Figure Captions

Figure 1. Plot of the radiance ratio (TES/AIRS) vs. radiance and color coded for frequency ranges. Panel (A) shows the spread in values over the homogenous cases for the baseline calibration in V001. Panel (B) shows this for the improved V002 L1B calibration.

Figure 2. TES/AIRS radiance comparison in the 2B1 filter for 50 cases for the TES Global survey 2147. The top panel shows the brightness temperature difference as a function of frequency average over 50 cases. The bottom panel shows the filter averaged TES-AIRS brightness temperature difference for each case as a function of time along the TES Global Survey.

Figure 3. TES/AIRS radiance comparison in the 1B2 filter, using the same plotting convention as Figure 2.

Figure 4. TES/AIRS radiance comparison in the 2A1 filter, using the same plotting convention as Figure 2.

Figure 5. Time series of normalized Integrated Spectral Magnitude (ISM) (top panel) and beam splitter temperature (bottom panel). The ISM is the area integration of the TES spectral radiance viewing the on-board hot calibration source and they are normalized to 1.0 at the beginning of the time series.

Figure 6. Plot of the TES 1A1 filter estimated NESBT (Noise Equivalent Source Brightness Temperature) values as a function frequency. Run 3194 is a TES global survey on November 27-28, 2005 just before the optical bench warm-up. Run 3202 is a TES global survey on December 7-8, 2005 just after the optical bench warm-up. Also, plotted for reference is Run 2298, which is the TES step-and-stare run used in the TES/SHIS comparisons. The criteria for the scans included in the plots are: latitudes between 20S and 20N, surface brightness temperatures between 290K and 295K, and screened with the TES master quality flag. Each plot is the average NESBT for TES scans that are each 15 pixel detector averages.

Figure 7. Brightness temperature in the $1103\text{--}1105\text{ cm}^{-1}$ microwindow for TES nadir-scans (Run 2298, Sequence 3, Scan 8 and Scan 10), each consisting of sixteen $0.5 \times 5\text{ km}^2$ rectangular pixels, and nine S-HIS scans for the corresponding underflight; SHIS scans are $\sim 2\text{ km}$ circles.

Figure 8. Same example TES nadir spectrum from November 7, 2004 for filters 2B1, 1B2, 2A1, and 1A1, but with the SHIS (red) and the TES spectral convolved with the SHIS ILS (blue) overplotted.

528

529 **Figure 9. Difference between TES and S-HIS brightness temperature residuals for Run**
530 **2298, Sequence 3, Scan 10 at the S-HIS resolution, for filters 2B1, 1B2, 2A1, and 1A1. TES**
531 **V002 L1B radiances were used in this comparison. The red regions are the TES**
532 **microwindows presently used in TES retrievals.**

533 **Figure 10. Scatter plots of TES-SHIS brightness temperature differences as a function of**
534 **brightness temperature and color coded in frequency bins, for Run 2298, Sequence 3,**
535 **Scans 8 and 10. The bold dashed lines are the 1-sigma standard deviation and the solid line**
536 **is the mean. TES V002 L1B radiances are used in the comparison.**

537 **Figure 11. Scatter plots of TES-AIRS brightness temperature differences as a function of**
538 **brightness temperature and color coded in frequency bins, for 43 global clear sky cases**
539 **over the ocean. The bold dashed lines are the 1-sigma standard deviation and the solid line**
540 **is the mean.**

541

542 **Figures**

543

544

545

546

547

548

549

550

551

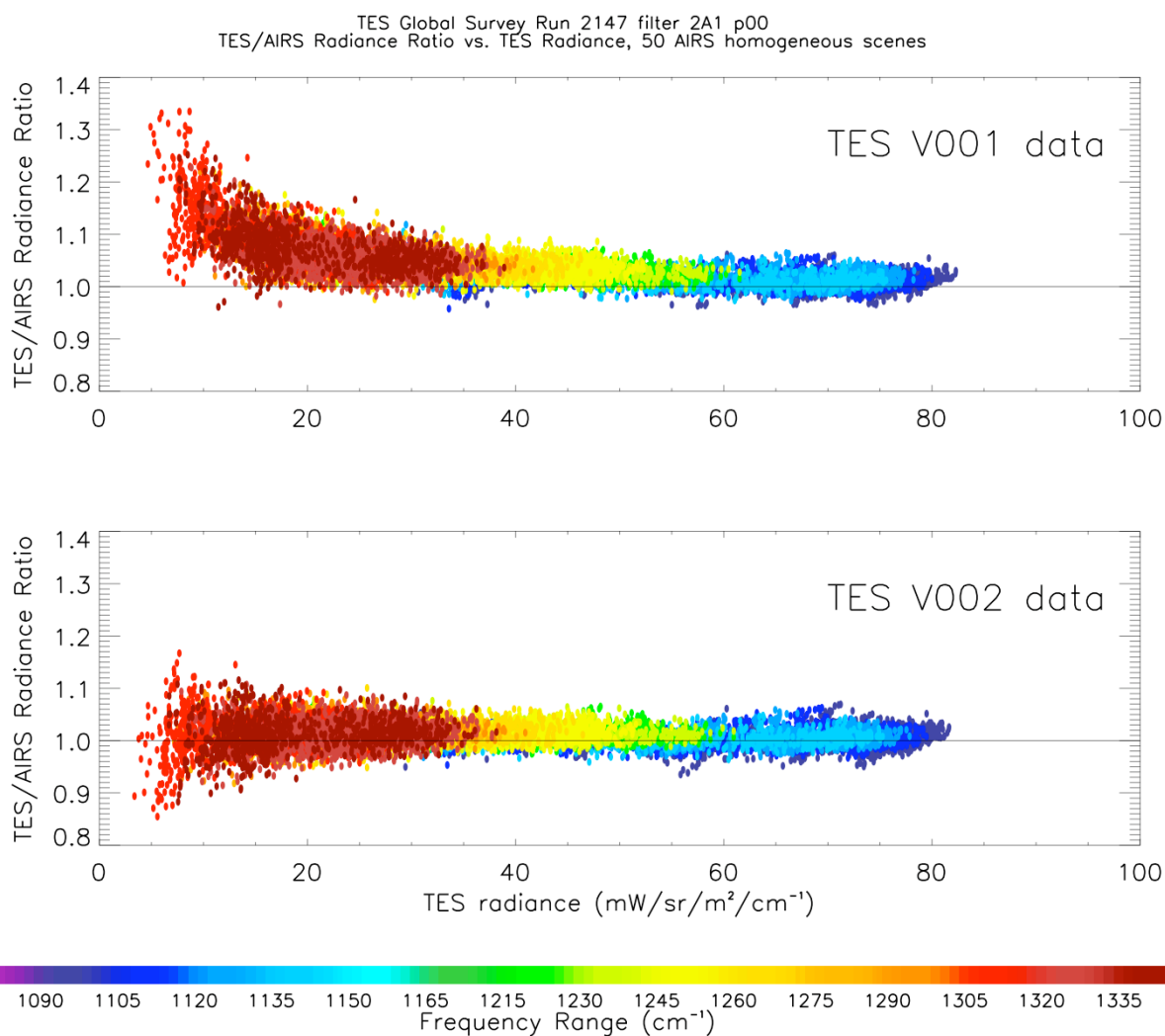
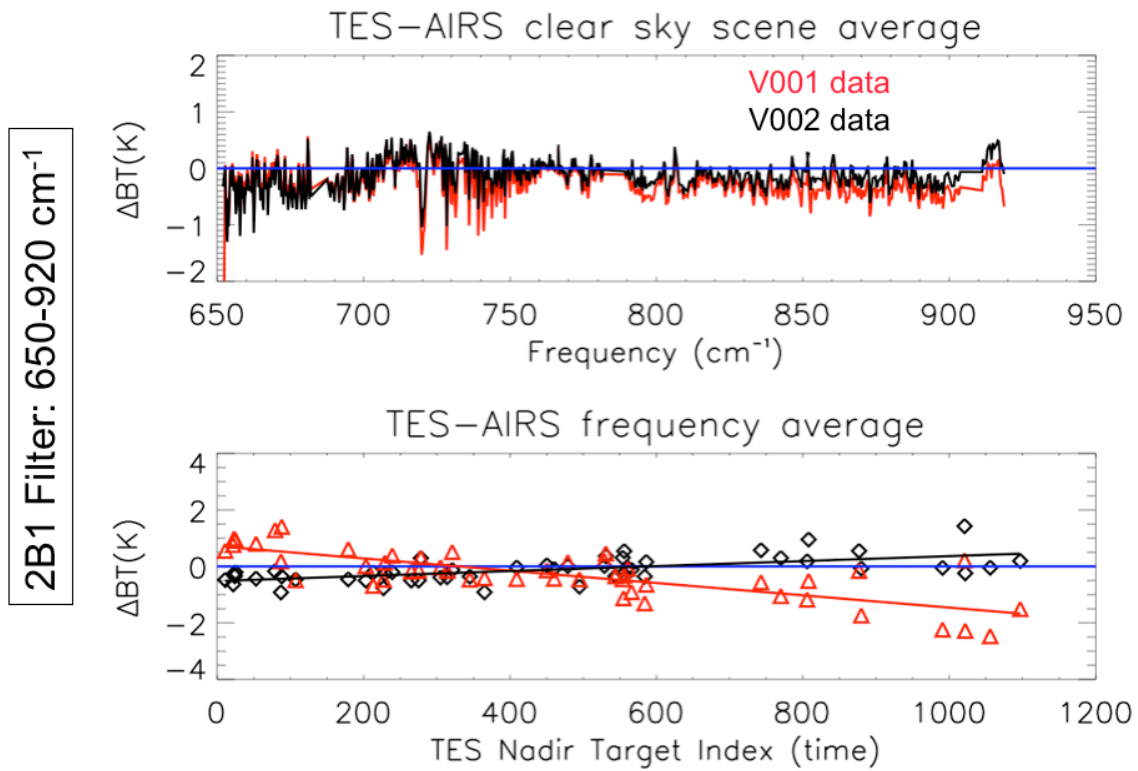
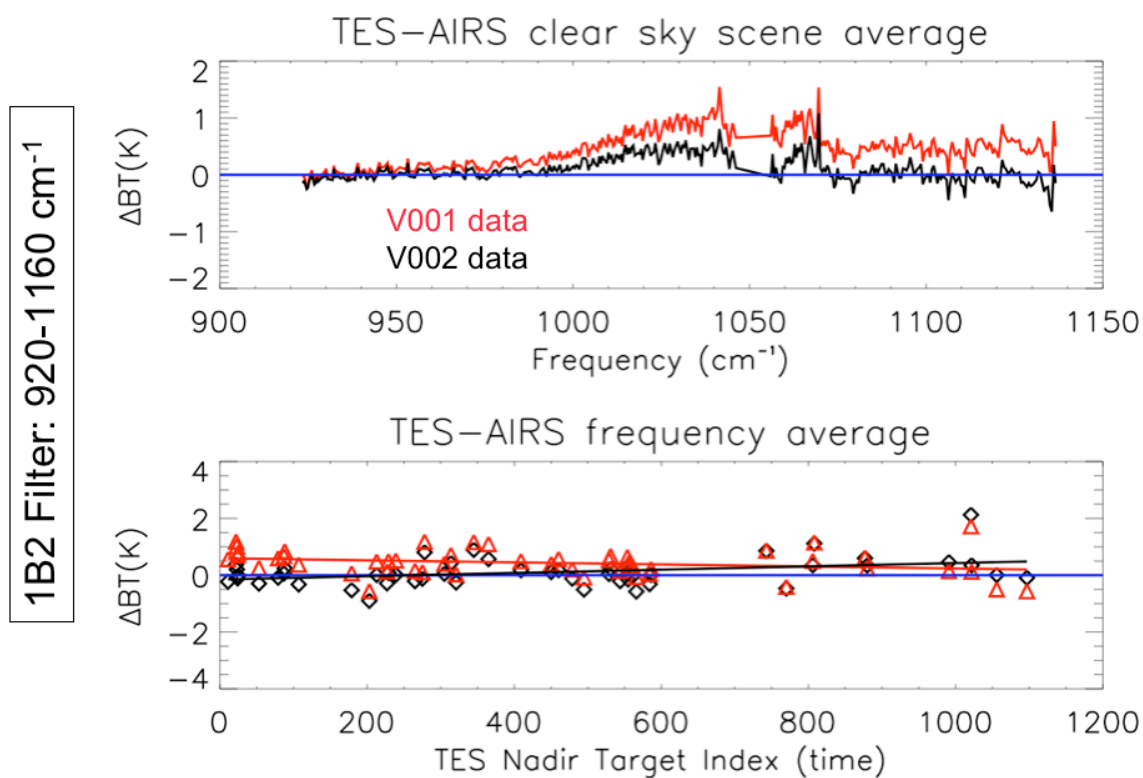


Figure 1. Plot of the radiance ratio (TES/AIRS) vs. radiance and color coded for frequency ranges. Panel (A) shows the spread in values over the homogenous cases for the baseline calibration in V001. Panel (B) shows this for the improved V002 L1B calibration.



2B1 Filter: 650-920 cm^{-1}

Figure 2. TES/AIRS radiance comparison in the 2B1 filter for 50 cases for the TES Global survey 2147. The top panel shows the brightness temperature difference as a function of frequency average over 50 cases. The bottom panel shows the filter averaged TES-AIRS brightness temperature difference for each case as a function of time along the TES Global Survey.



570

571 **Figure 3. TES/AIRS radiance comparison in the 1B2 filter, using the same plotting**
 572 **convention as Figure 2.**

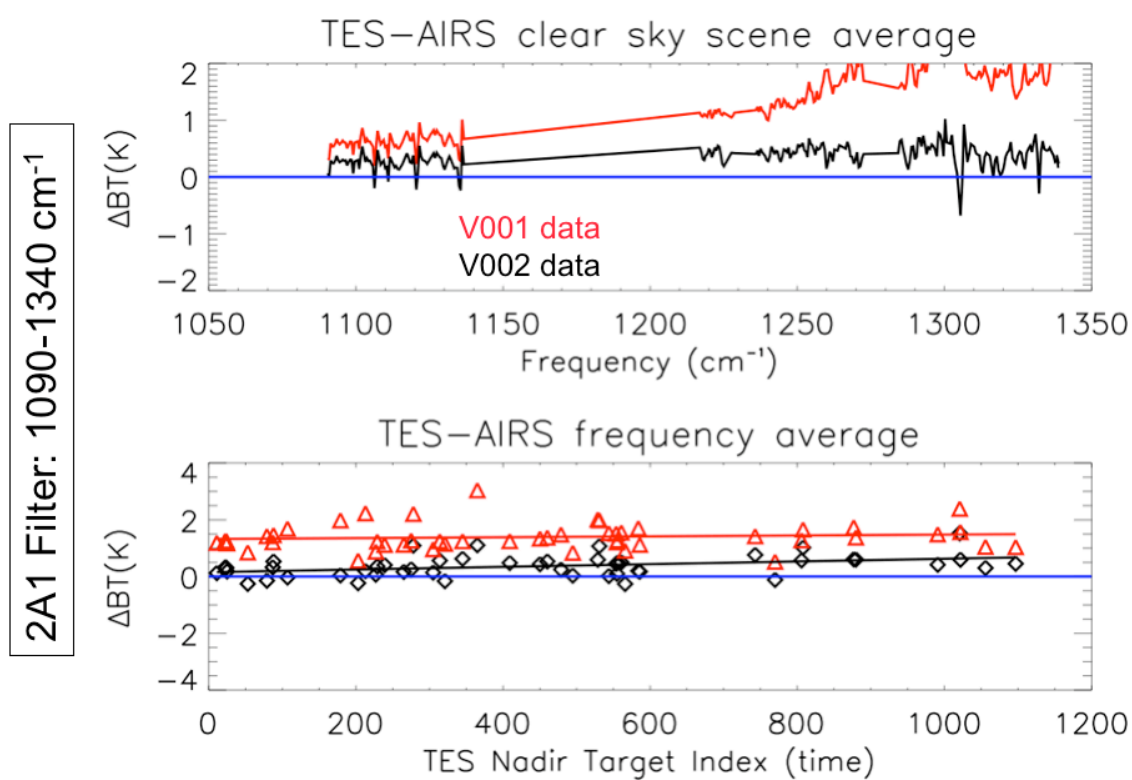


Figure 4. TES/AIRS radiance comparison in the 2A1 filter, using the same plotting convention as Figure 2.

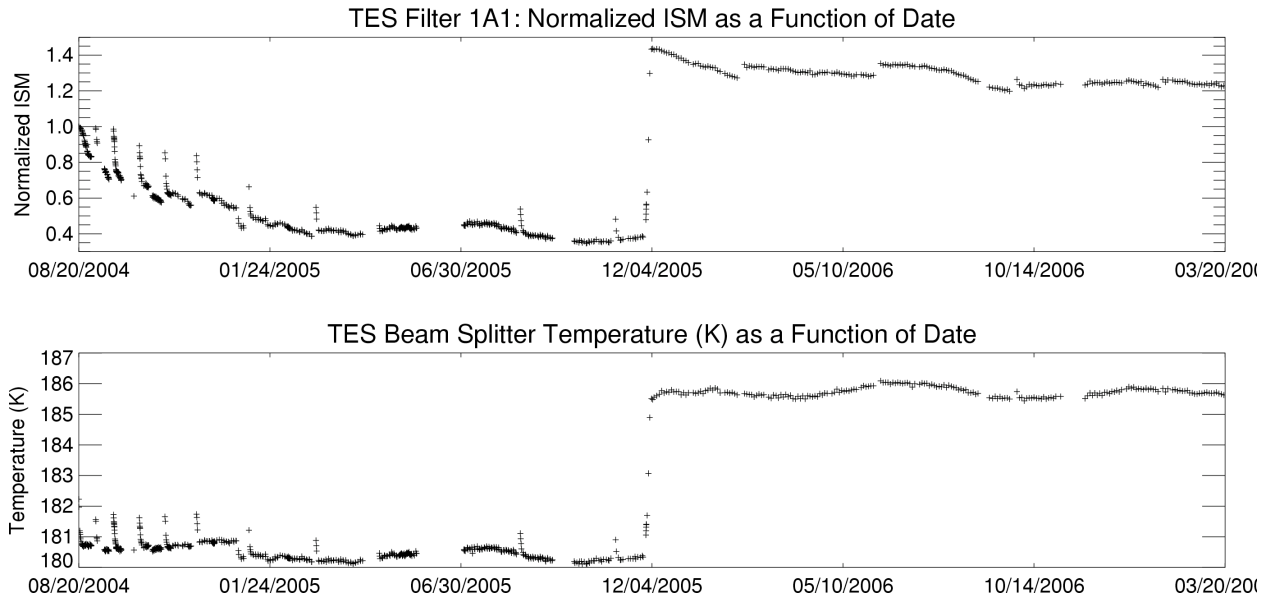


Figure 5. Time series of normalized Integrated Spectral Magnitude (ISM) for TES filter 1A1 (top panel) and beam splitter temperature (bottom panel). The ISM is the area integration of the TES spectral radiance viewing the on-board hot calibration source and they are normalized to 1.0 at the beginning of the time series.

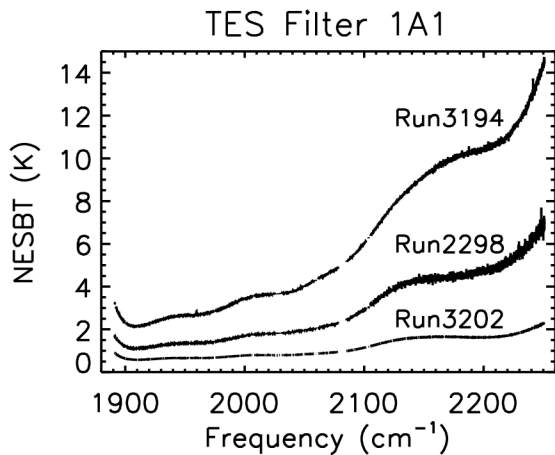


Figure 6. Plot of the TES 1A1 filter estimated NESBT (Noise Equivalent Source Brightness Temperature) values as a function frequency. Run 3194 is a TES global survey on November 27-28, 2005 just before the optical bench warm-up. Run 3202 is a TES global survey on December 7-8, 2005 just after the optical bench warm-up. Also, plotted for reference is Run 2298, which is the TES step-and-stare run used in the TES/SHIS comparisons. The criteria for the scans included in the plots are: latitudes between 20S and 20N, surface brightness temperatures between 290K and 295K, and screened with the TES master quality flag. Each plot is the average NESBT for TES scans that are each 15 pixel detector averages.

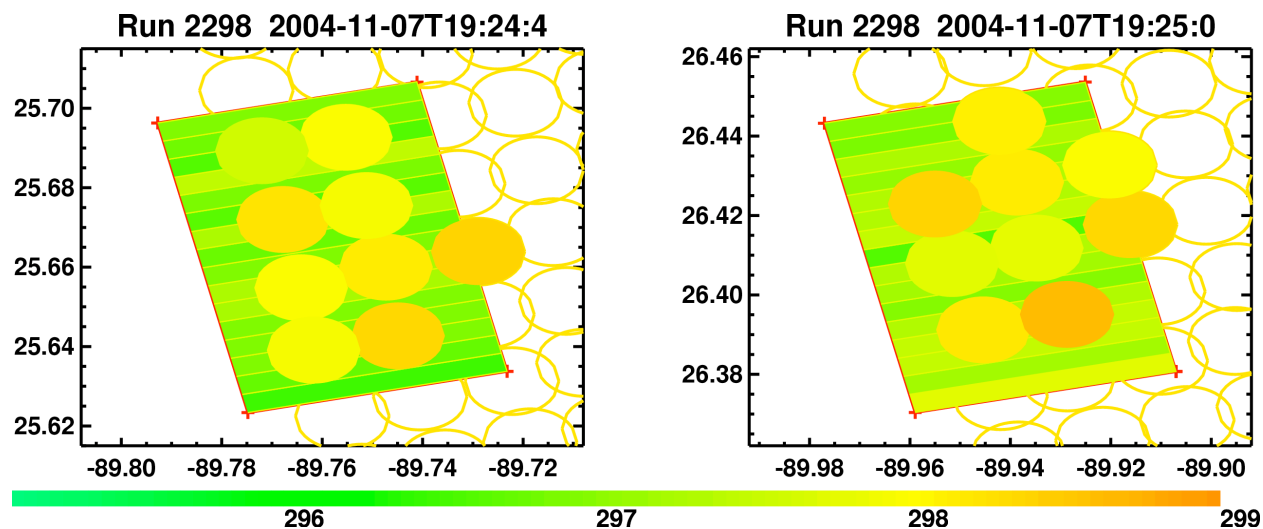


Figure 7. Brightness temperature in the 1103-1105 cm⁻¹ microwindow for TES nadir-scans (Run 2298, Sequence 3, Scan 8 and Scan 10), each consisting of sixteen 0.5 x 5 km² rectangular pixels, and nine S-HIS scans for the corresponding underflight; SHIS scans are ~2 km circles.

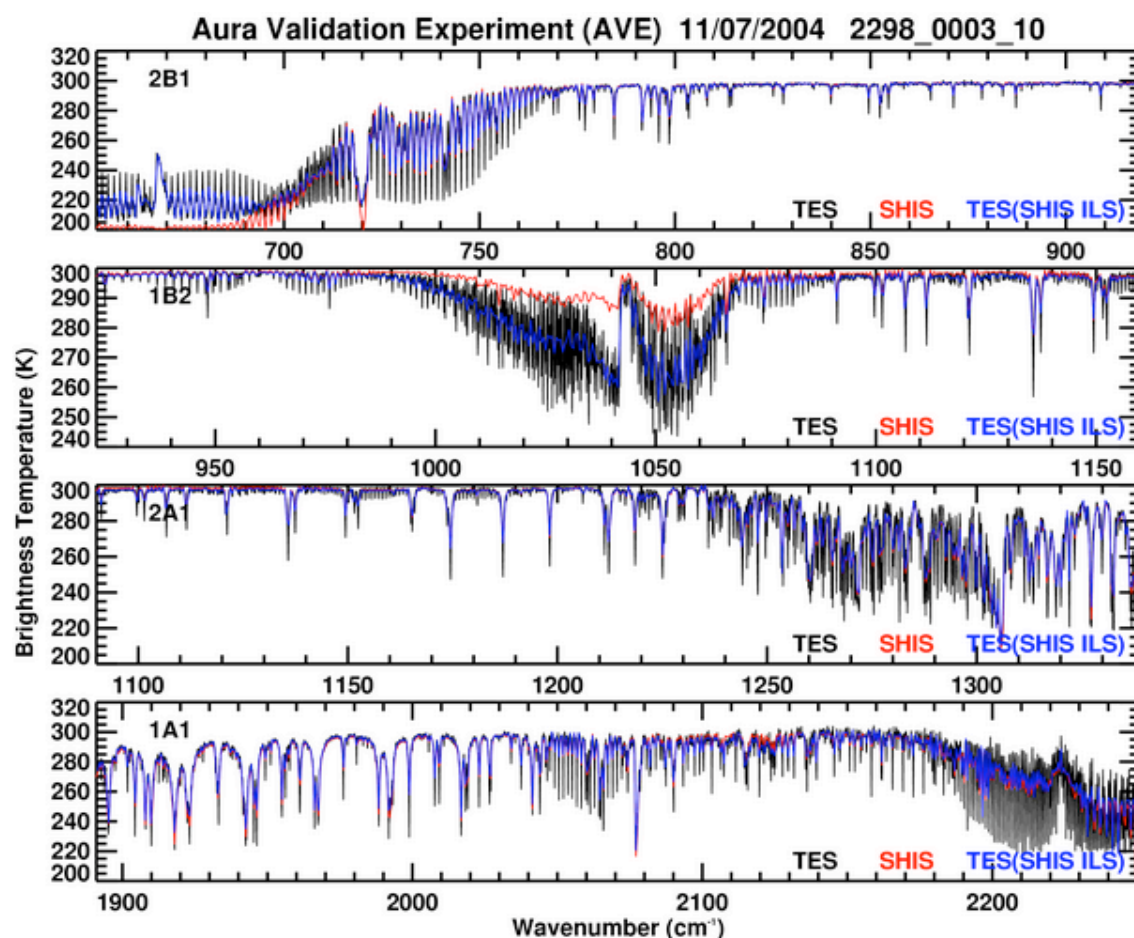


Figure 8. TES nadir spectrum from November 7, 2004 for filters 2B1, 1B2, 2A1, and 1A1, with the SHIS (red) and the TES spectral convolved with the SHIS ILS (blue) overplotted.

TES/SHIS AVE Comparisons 11/07/2004 2298_0003_10

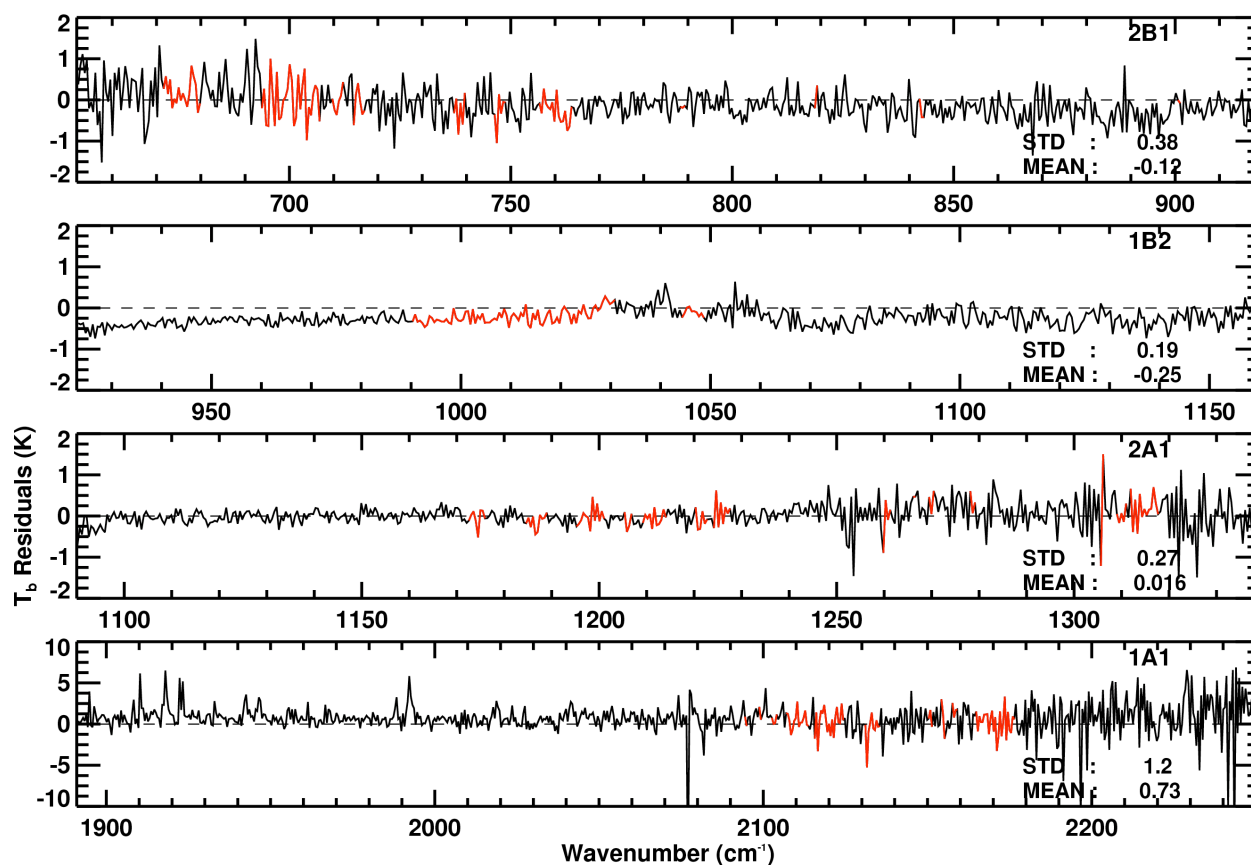


Figure 9. Difference between TES and S-HIS brightness temperature residuals for Run 2298, Sequence 3, Scan 10 at the S-HIS resolution, for filters 2B1, 1B2, 2A1, and 1A1. TES V002 L1B radiances were used in this comparison. The red regions are the TES microwindows presently used in TES retrievals.

TES/SHIS AVE Comparisons

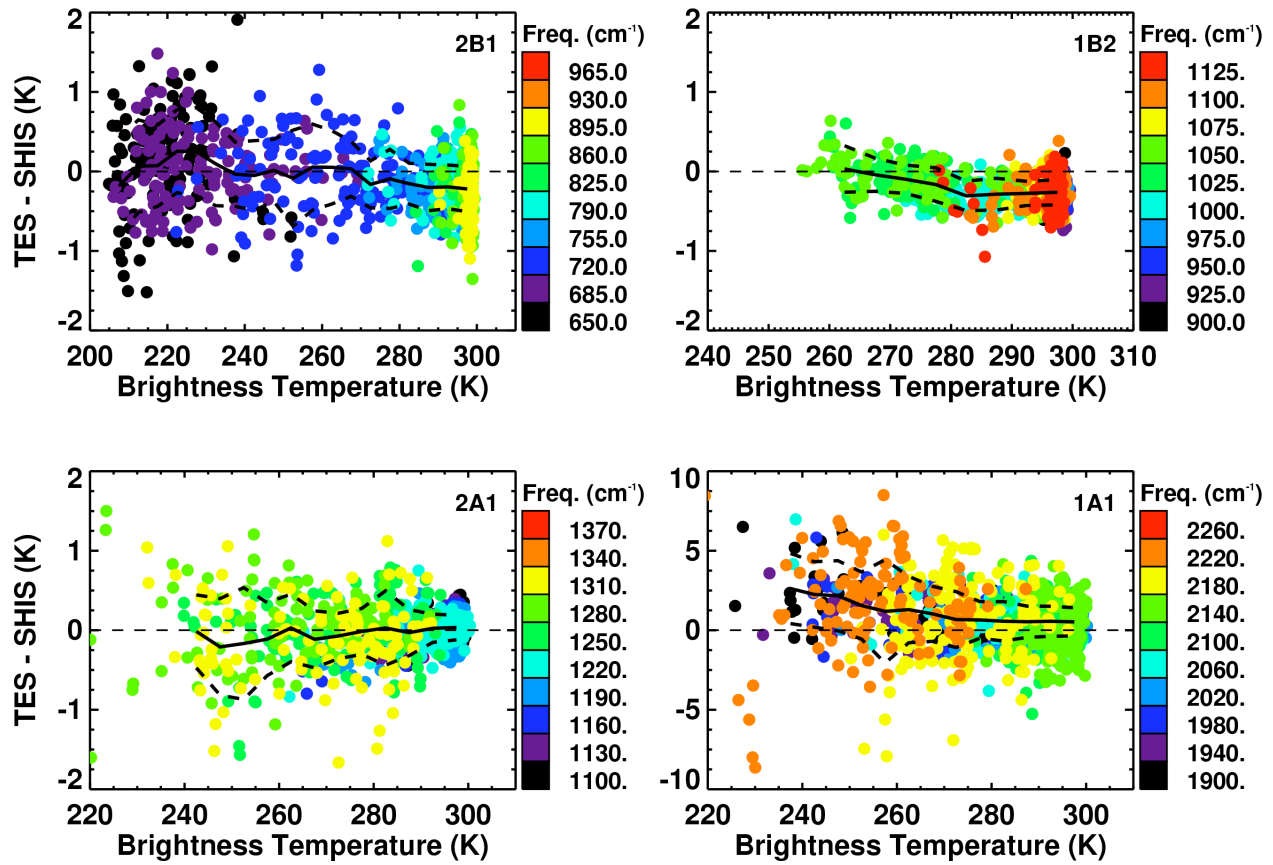


Figure 10. Scatter plots of TES-SHIS brightness temperature differences as a function of brightness temperature and color coded in frequency bins, for Run 2298, Sequence 3, Scans 8 and 10. The bold dashed lines are the 1-sigma standard deviation and the solid line is the mean. TES V002 L1B radiances are used in the comparison.

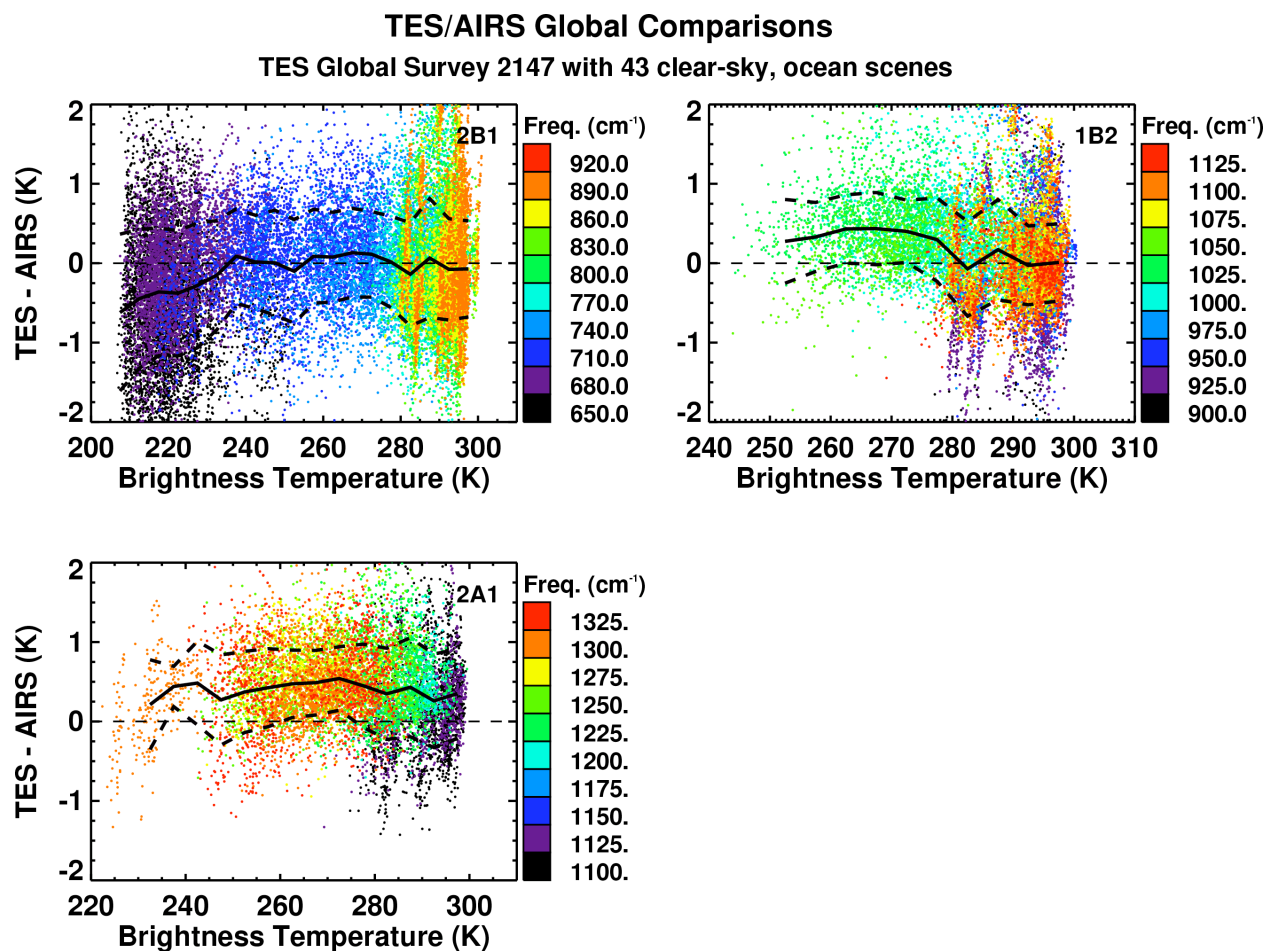


Figure 11. Scatter plots of TES-AIRS brightness temperature differences as a function of brightness temperature and color coded in frequency bins, for 43 global clear sky cases over the ocean. The bold dashed lines are the 1-sigma standard deviation and the solid line is the mean.

657

658

659

660

661